J Mater Sci: Mater Electron (2006) 17:951–962
DOI 10.1007/s10854-006-0036-x

# Microstructure development and electrical properties of $RuO_2$-based lead-free thick film resistors

**M. G. Busana · M. Prudenziati · J. Hormadaly**

Received: 30 March 2006 / Accepted: 12 June 2006


**Abstract** Lead-free thick film resistive compositions suitable for hybrid microelectronics were prepared. The compositions were made with $RuO_2$ as the conducting phase and bismuthate glasses. This blend of bismuthate glasses constitutes a suitable choice for avoiding negative effects such as devitrification, bleeding out of the glass on alumina substrates, anomalous distribution of conductive grains in the glassy matrix and phase separation observed in other systems. The morphology, microstructure and electrical properties have been studied. X-ray diffraction (XRD), electron scanning microscopy (SEM) and energy dispersion spectroscopy (EDS) show that a defect pyrochlore phase of bismuth titanate formed at about 700 °C in all the compositions studied. Transmission electron microscopy (TEM) analysis of the original $RuO_2$ powder shows that a single grain is made of many smaller grains of different crystalline orientations. The sheet resistance spans two decades by changing the $RuO_2$ fraction from about 14–52 wt%. The resistors exhibit good reproducibility and their temperature coefficient of resistance is in the range of ± 300 ppm/°C.

M. G. Busana · M. Prudenziati (✉)
Department of Physics, University of Modena,
via G. Campi, 213/A, 41100 Modena, Italy
e-mail: Prudenziati.maria@unimo.it

J. Hormadaly
Zandman Center for thick film microelectronics and
Department of Chemistry, Ben-Gurion University of the
Negev, Beer Sheva, Israel
e-mail: hormadj@bgumail.bgu.ac.il

## 1 Introduction

In response to the demand for lead-free processing, to reduce negative environmental effects resulting from disposal of electronic products and to conform to the relevant legislation, the electronics industry has been engaged for several years in the development of new lead-free materials. As a result, lead-free products are currently available for solders, packaging and thick-film conductive pastes for interconnections and contacts of components. However, the development of lead-free compositions for thick-film hybrid microelectronics is not a simple task, and only partially satisfactory compositions [1–6] based on the usual conductive phases (ruthenium dioxide and perovskite ruthenate) have been obtained for lead-free thick film resistors (TFRs).

In this paper, we report the development of lead-free $RuO_2$-based TFR compositions in bismuthate glasses. The glasses were chosen so as to avoid the negative effects observed in other systems, such as devitrification, bleeding of the glass on alumina substrates, anomalous distribution of conductive grains in the glassy matrix and phase separations. The morphology, microstructure and electrical properties of the materials were determined. Resistors with low sheet resistance and with suitable electrical properties were produced from the developed compositions.

## 2 Experimental

### 2.1 Glasses, additives and resistor formulations

Three resistor compositions denoted as JH024/3, JH024/4 and JH024/5 were the subject of this study.

The basic glass composition used in the resistor formulations was a bismuthate glass detailed on US Patent 6,171,987 B1 [7] in example No. 29. Additives and modifications of this glass for each paste are described below. Glass frits were ground with deionized water to give fine powders with mean particle size $\leqslant 10\mu$m.

Additives used were of two types:

(1) TCR drivers, oxides or complex oxides which modify the TCR, generally lowering the TCR, such as $TiO_2$, $Nb_2O_5$ and $Mn_2O_3$.
(2) Inert fillers such as $SiO_2$ and $ZrSiO_4$ which are used to reduce resistor expansion and increase abrasion resistance.

Additives can be incorporated in the glass or added as oxides to the resistor formulations.

Resistor formulations were obtained by mixing the appropriate ratios of glasses, conducting phase ($RuO_2$, surface area of 20 $m^2$/g, corresponding to a mean diameter $D = 430$ Å for spherical grains), standard organic vehicle (a solution of ethyl cellulose in terpineol dibutyl carbitol) and additives which pyrolize completely [8]. The mixture was dispersed on a three-roll mill to yield a fine paste with the desired grind gauge and viscosity. The conducting phase content was varied between ~14 and 52 wt% to obtain decade resistance values of ~10 Ω/□, ~100 Ω/□ and ~1 kΩ/□. The TCR drivers were adjusted to yield formulations with low and acceptable TCR values.

## 2.2 Powders

Conducting phase powders was separated from the fired resistor to study size, chemical and morphological changes. The procedure involved heating a paste sample in a Pt/Rh crucible employing the same firing schedule used for the fabrication of the resistor films. The fired pastes did not adhere to the crucible; they were ground in an agate mortar to form fine powders. Powders were treated with a solution containing $HNO_3$ (70%):HF (52%):$H_2O$ at a volume ratio of 1:3:10, respectively. The mixed acid composition was reported [9] to dissolve lead-borosilicate glassy phase without affecting crystalline phases. With the bismuthate glasses of this study, the acid mixture did not leach the glassy phase completely; therefore the etched powders were subjected to another acid solution of HCl (37%) in water, 1:20 by volume. The conducting phase powders obtained after etching were analysed with X-ray diffraction (XRD), scanning electron microscopy and energy dispersive spectroscopy (SEM-EDS). The original $RuO_2$ powder was observed in transmission electron microscopy (TEM).

## 2.3 Resistive layers, resistors and measurement of electrical properties

The pastes were screen printed onto 96% alumina substrates (Hoechst CeramTec 700) and fired. Large samples ( $>10 \times 10$ $mm^2$) were prepared to perform 4-point probe measurements of resistance, XRD and SEM-EDS analyses either in plane or in cross-sections. Each paste composition was screen printed to fabricate several samples of the large pattern. Samples were fired at various peak temperatures ($T_f$) in the range of 650–900 °C, in steps of 50 °C. The firing process was performed in a BTU six-zones belt furnace (model QA41654). Resistors were fabricated by screen printing paste on alumina substrates with Pt/Au prefired terminations. Various patterns were prepared: (a) eight resistors of constant width (2 mm) and variable length ranging from 0.5 to 10 mm for measuring the size effect (i.e. the change in effective sheet resistance relative to the change of the resistor length) and (b) square resistors $1 \times 1$ $mm^2$ in size for measuring the temperature dependence of resistance.

Firing was done in the belt furnace described above. The sheet resistance of fired layers was measured with the 4-point probes technique; the measuring system consisted of a current generator (Keithley 220), a digital multimeter (Philips PM2528) and a four point jig (Jeadel). The temperature dependence of resistance was measured in a cryogenic apparatus in the range of 4–400 K. The measurements were performed on $1 \times 1$ $mm^2$ resistors with Pt/Au terminations and on larger resistive layers $1.5 \times 1.5$ $cm^2$.

## 2.4 Analytical methods

SEM and elemental analysis (EDS) were performed with a Philips XL-40 microscope equipped with an Everhart Thornley detector (SED images) and solid state detector for backscattered electrons (BSD images). The EDS system includes an Oxford-satw Si(Li) detector and the X-EDS Oxford INCA software. Unless otherwise mentioned the energy of the electron beam impinging on the sample was $E = 25$ keV; however $E = 12$ keV was used to gain compositional information from reduced sample volume.

XRD patterns were collected with a Panalytical $\theta$-$\theta$ diffractometer (Ni-filtered Cu$K_\alpha$ radiation, $\lambda = 1.544$ Å) equipped with an X'Celeretor and a chamber Anton Paar HTK16 designed to perform in situ analyses up to 1,600 °C. Data were collected in the angular region of 10°–90° in 2$\theta$-step scanning mode. The conditions included: filament current 40 mA, 40 kV and step size of 0.01°; sample time was variable according

to the scope and type of the samples investigated. The spectra were analysed with the X'PERT High Score Plus programme and the incorporated database for phase identification. From the half-width line broadening, the diameter $D$ of the $RuO_2$ grains was computed with the Scherrer formula [10]

$$D = \frac{K\lambda}{\beta \cos \vartheta} \quad (1)$$

where $\beta$ is the corrected line width, $\theta$ the peak position and $k = 1$.

Images were collected and analysis performed on the original $RuO_2$ powders with the Joel 2011 TEM operated at 200 kV; the microscope was equipped with a GIF GATAN 794 CCD camera, Digital Micrograph 3.4 software and the INCA 100 microanalysis system link.

## 3 Results and discussions

### 3.1 Pastes

Figure 1 shows the BSD image of the inorganic constituents of paste JH024/3. The glass particles are bright in color (because of the high bismuth content), show sharp edges and range in size form about one to several microns. The grey particles, rich in zirconium and silicon were identified as $ZrSiO_4$. Finer (submicron size) and nearly spherical grains rich in Ru were identified as $RuO_2$. Identification of phases is supported by EDS and XRD. The large black regions in Fig. 1 correspond to uncovered areas of alumina substrate. Similar images were observed for the other two pastes JH024/4 and JH024/5. Aside from the major detectable elements (O, Ru, Bi, Si) described above, the EDS analysis shows the following minor constituents:

Zn, Ti, Al, Nb, Mg, Zr and Mn in JH024/3
Zn, Ti, Al, Nb, Mg, Zr and Mn in JH024/4
Zn, Ti, Al, Nb, Mg and Mn in JH024/5
$ZrSiO_4$ was not detected in JH024/5.

### 3.2 Powders

#### *3.2.1 XRD*

XRD analyses performed on powders originating from JH024/3 and JH024/4 (organic vehicle removed by dissolving it in acetone) were subjected to two heat treatments 500 and 850 °C. XRD patterns for JH024/3 and JH024/4 were similar, hence only the results for JH024/3 are discussed. Figure 2 shows the XRD pattern of powder subjected to 500°C heating. The XRD pattern shows the typical hump for vitreous phase and lines for $RuO_2$, $ZrSiO_4$ and $SiO_2$ phases.

Figure 3 shows the XRD of JH024/3 powder subjected to 850°C heat treatment. The figure shows the development of new cubic phase (a pyrochlore) and lines of $Zn_2$ $SiO_4$ phase which might form by crystallization of the bismuthate glasses. Compositional identification of the pyrochlore phase follows after the results for powder extracted from JH024/5.

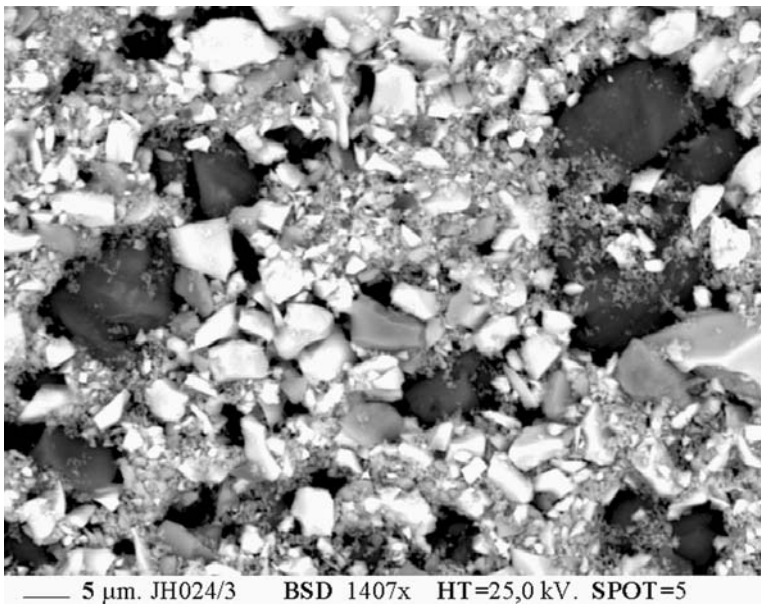


**Fig. 1** SEM-BSD micrograph of JH024/3 ink

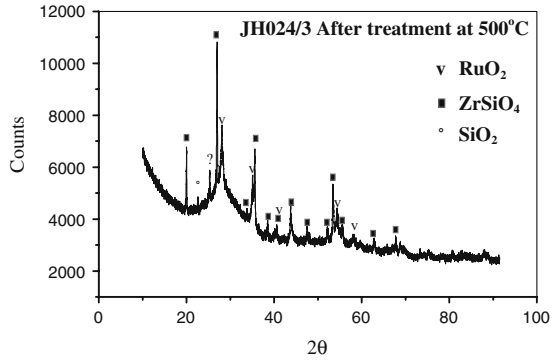


**Fig. 2** XRD pattern of powder from sample JH024 /3. The pattern of sample JH024/4 differs only in the higher relative counts for the $RuO_2$ peaks

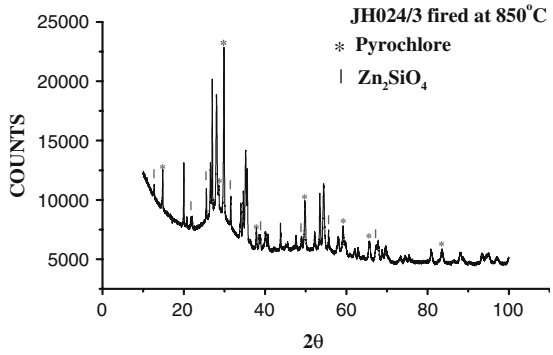


**Fig. 3** XRD pattern of the sample JH024/3 heated to 850 °C

XRD patterns of powder extracted from JH024/5 shows that zircon is absent from the 500 °C to the 850 °C heat treatments. Absence of zircon supports the EDS analysis performed on the paste (Section III.1). XRD of JH024/5 powder after 850°C firing shows lines attributed to the pyrochlore phase, the lines are shifted (higher $2\theta$ values) relative to powders of JH024/3 and JH024/4. More details for the evaluation of the cubic phase were obtained by XRD analysis of powders in the hot stage apparatus. Temperature was increased by 25 °C increments from 650 to 1,100°C; real temperatures on the powders ranged from 630 to 910°C. For each temperature increase the XRD pattern was recorded in the $2\theta$ range of 25° to 32°. The XRD patterns show that the pyrochlore phase starts to form at about 700 °C in JH024/3 and JH024/4 powders and at 750 °C in JH024/5. The peaks show a monotonous increase in intensity with temperature and simultaneously peak widths decrease. These trends indicate the amount of the crystalline phase and its grains size increase with temperature. Similar features (increase of peak height and narrowing of the peak width, see Table 1) were also observed for the main $RuO_2$ peak,

**Table 1** FWHM of the peak ($2\theta$ = 28.05) for $RuO_2$ (sample JH024 /5)

| $T$ [°C] | FWHM |
|---|---|
| 650 | 0.40 |
| 700 | 0.36 |
| 750 | 0.35 |
| 790 | 0.34 |
| 810 | 0.32 |
| 850 | 0.29 |
| 890 | 0.23 |
| 910 | 0.20 |

but the area under this peak remained essentially constant (at least up to 890 °C). These features have previously been observed in $RuO_2$-based resistors having a Pb-bearing matrix and their formation has been ascribed to the sintering and/or Oswald ripening responsible for an increase in grain size [11].

In all compositions tested the phase $Bi_4Si_3O_{12}$ formed (responsible for the peak at $2\theta$ = 27.4); its maximum intensity was found at $T$ = 810 °C but this phase disappears at about $T$ = 890°C. This phase crystallizes from the bismuthate glasses in the temperature range of 700–890°C and at higher temperature it dissolves in the glass.

### *3.2.2 Etching in HCl*

Resistor powders, which were fired as described above, were subjected to etching in hydrochloric acid according to the procedure described in the experimental section. After etching the vitreous hump in the XRD disappeared, an indication that the glassy phase was removed, the reflections from the remaining crystalline phases were the same as in the non-etched samples. SEM-EDS analysis confirmed the selective dissolution of the glassy phase and facilitated chemical identification of the grains rich in Bi, Ti and O (Bi:Ti atomic ratio 1:1). Two grains are indicated with arrows in Fig. 4, which shows the BSD image of etched JH024/3 sample. Fig. 5 shows elemental maps of these grains. The maps clearly show correlation between Bi and Ti and also show no Ru in the newly formed phase.

The results of the previous sections show that a new cubic phase is formed during heating. Since no Ru is found in the grains of the new phase and the XRD patterns of $RuO_2$ phase do not show a decrease in $RuO_2$ content as a function of temperature, Ru pyrochlore formation is ruled out. The XRD patterns of JH024/3 and JH024/4 samples fired at 800°C are in excellent agreement with published patterns of distorted $Bi_2Ti_2O_7$ pyrochlore phase [12–14]. However, at 850 °C firing, the XRD patterns of the same samples

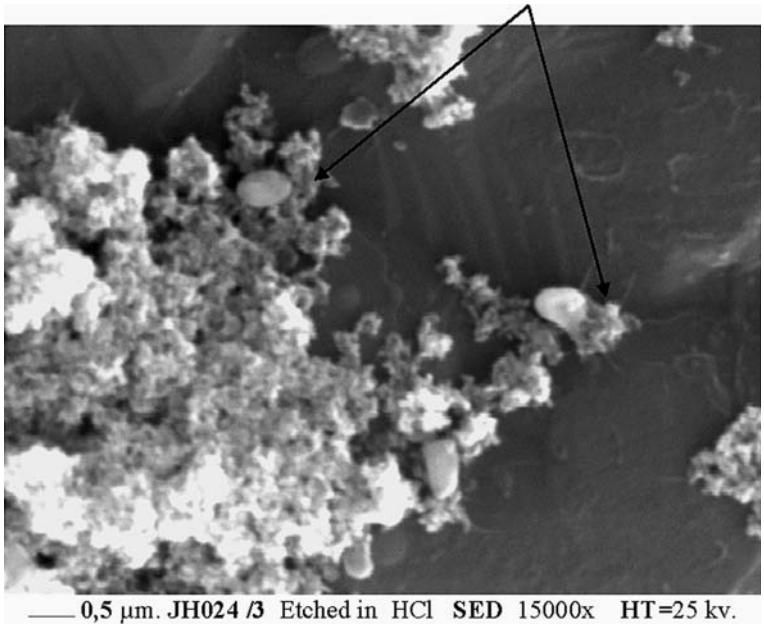


**Fig. 4** Powder JH024/3 first heated at 900°C and then chemically etched in HCl

agree better with the pattern of the non-stoichiometric $Bi_{1.74}Ti_2O_{6.62}$ [12]. The Bi/Ti atomic ratio measured in this study (EDS) is given in Table 2. The shift in the $2\theta$ values of the new cubic phase as a function of the firing temperature, indicates a change in the cell constant of the cubic phase. The resistor compositions of this study contain several oxides, which can be accommodated in the A and B sites of the pyrochlore structure (general formula of the pyrochlore is $A_2B_2O_6O'$ where A has a coordination number of eight and typically has trivalent, divalent and monovalent ions, while the B site has a coordination number of six and can accommodate ions with a variety of oxidation states). $Zn^{2+}$, $Bi^{3+}$ and $Mg^{2+}$ can occupy the A site and $Ti^{4+}$, $Nb^{5+}$ and $Zr^{4+}$ can be accommodated by the B site. Based on the data of this study, we can only conclude that a pyrochlore compound of the general composition $Bi_{2-x-y}$ $Zn_x$ $Mg_y$ $Ti_{2-u-v}$ $Nb_u$ $Zr_v$ $O_{7-\delta}$ is formed during heating of the resistor compositions and x, y, u and v are functions of the heat treatment.

### *3.2.3 TEM*

A high-resolution TEM of a single grain of the original $RuO_2$ (Fig. 6) shows that this grain is comprised of sub-grains of different crystalline orientation. In fact, atomic layers of different orientations are evident in the image. Fourier analysis of the electron density in this image clearly shows the polycrystalline structure of the single grain. This finding enables us to reconcile the difference in values of grain sizes observed by different techniques (SSA, XRD and SEM).

Evaluation of the $RuO_2$ grain size, based on the Debye–Sherrer formula and the data reported in Table 1, indicates a growth of the grains from 220 Å (original $RuO_2$ powders as well as $RuO_2$ in dried pastes) to 630 Å (samples fired at $T_f = 910°C$). The discrepancy between the value obtained from XRD line broadening (220 Å) and the BET measurement (430 Å for spherical grains, Section III.2. 1) for the unheated powders is much larger than the evaluated relative accuracy of the two measurements. This discrepancy may be explained by taking into account various concomitant effects, as follows [11]:

(a) Very small particles have a marked tendency to agglomerate into clusters; hence in BET measurements the grains are ''seen'' as larger than the single crystallites which contribute to the X-ray line broadening.
(b) The X-ray peak width may underestimate the grain size because of crystallographic defects.
(c) Small particles are sponge-like, which contributes to a larger surface area than in spherical particles.

All these considerations are valid for submicrometer-sized powders, but in the present study point (b) is more than simply an assumption: the high resolution TEM image (Fig. 6) shows clearly that a single $RuO_2$ grain is made of a multiplicity of sub-grains (different crystallographic domains). This observation also implies that the decrease in width of the X-ray reflection lines caused by increasing the firing temperature might be due not only to grain growth (from sintering

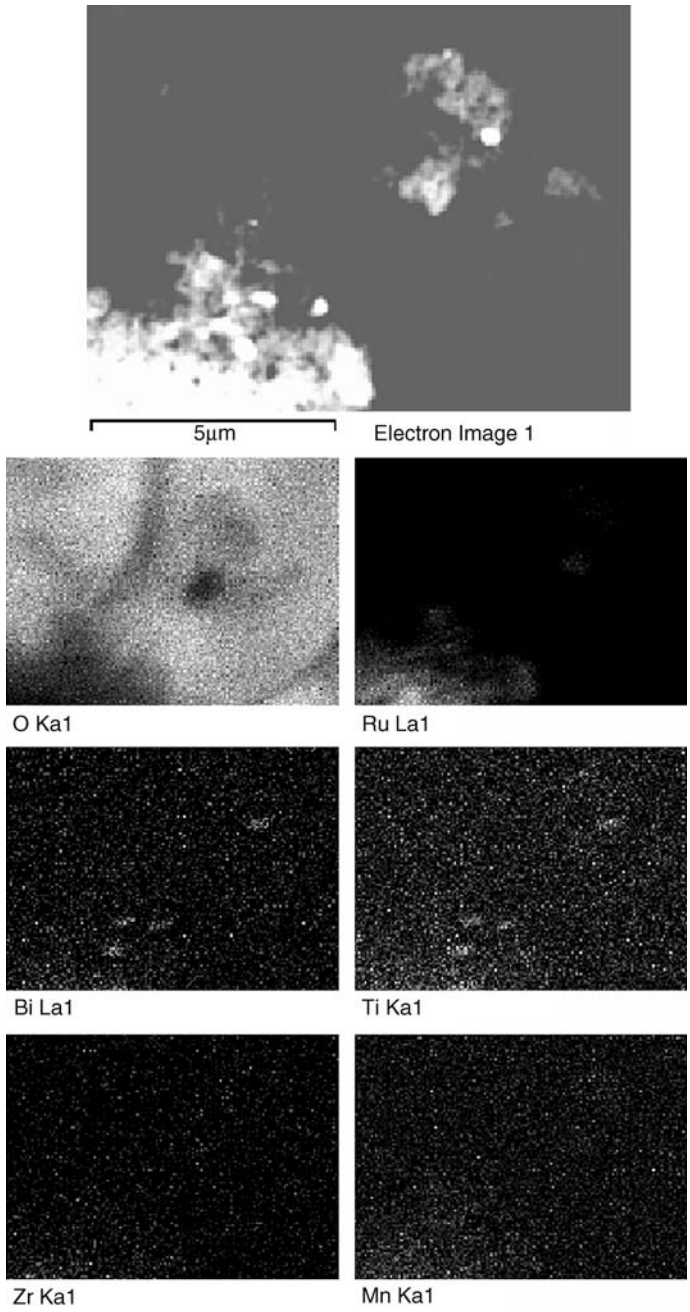


**Fig. 5** BSD image and elemental maps of the same area as that shown in Fig. 4

and Oswald ripening of different grains), but also to the rearrangement of the crystallographic lattice inside separated grains. This is an interesting hypothesis which deserves further study.

## 3.3 Resistive layers

### *3.3.1 XRD*

XRD analysis of resistive layers either dried at 500°C or fired at 850 °C did not differ substantially from that of comparably heated powders. It is therefore obvious that possible interactions between the ink components and the alumina substrate did not result in the formation of new phases.

Figure 7 compares XRD patterns of resistive layers prepared with the JH024/3 ink. The patterns show changes in height and width of the peaks due to $RuO_2$ and the pyrochlore phase. In addition, the presence of $Bi_4(SiO_4)_3$ is evident in samples fired at $T_f = 800$°C. This phase was not observed in samples prepared from the other inks (JH024/4 and JH024/5).

**Table 2** Bi/Ti atomic ratio measured in JH024/3 and JH024/4 (powders heated at 900°C) and, for comparison, the same ratios in compounds $Bi_2Ti_2O_7$ and $Bi_{1,74}Ti_2O_{6,62}$

| Compound/sample | Bi/Ti atomic ratio |
|---|---|
| $Bi_2Ti_2O_7$ | 1 |
| $Bi_{1.74}Ti_2O_{6.62}$ | 0.87 |
| JH024/3 (900 °C) | 0.9 |
| JH024/4 (900 °C) | 0.9 |

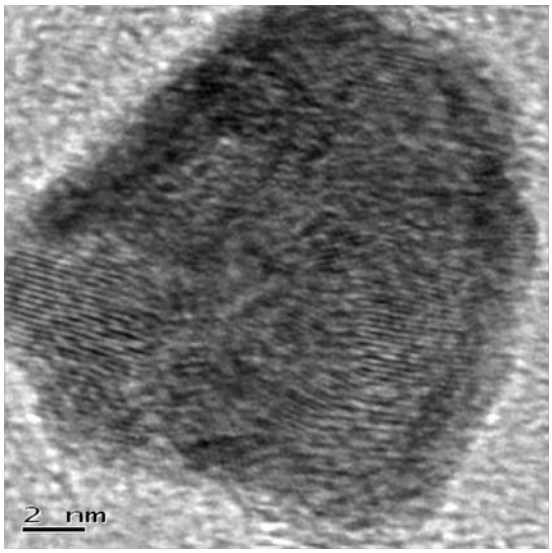


**Fig. 6** High resolution TEM image of a single $RuO_2$ grain from the original powder

**Fig. 7** XRD patterns for JH024/3 layers prepared on alumina at various peak firing temperatures $T_f$

Figure 8 shows the interplanar distance d(222) measured from the strongest peak of the pyrochlore phase measured at room temperature for layers prepared at various peak firing temperatures.

### *3.3.2 SEM-EDS*

SEM-EDS analyses were performed to evaluate developmental stages, homogeneity, porosity and distribution of the different phases. These analyses were also intended to determine whether these Pb-free resistors exhibit the ''standard segregation'' of $RuO_2$ grains around dielectric regions common to all traditional resistor compositions [15]. Qualitatively similar results were obtained for samples of the compositions JH024/3 and JH024/4.

*JH024/3*

For firing processes up to $T_f = 650°C$, no apparent development of the resistor microstructure was observed, i.e. no softening of the glass and no change in the distribution of inorganic particles. At $T_f = 700°C$ the sharp edges the glass particles disappeared and sintering necks became visible (Fig. 9). Between $T_f = 750°C$ and $T_f = 800°C$, the system densified progressively, and at $T_f = 850°C$ the glassy matrix was relatively compact, but with large pores. The $RuO_2$ grains were homogeneously embedded in the glassy matrix. Pores were also present inside the layer, as observed in cross-sectional views (Fig. 10), and did not vanish even after firing at temperatures up to 900°C (Fig. 11).

Elemental maps are given in Fig. 12 for the sample fired at $T_f = 850°C$. It is apparent that elements like

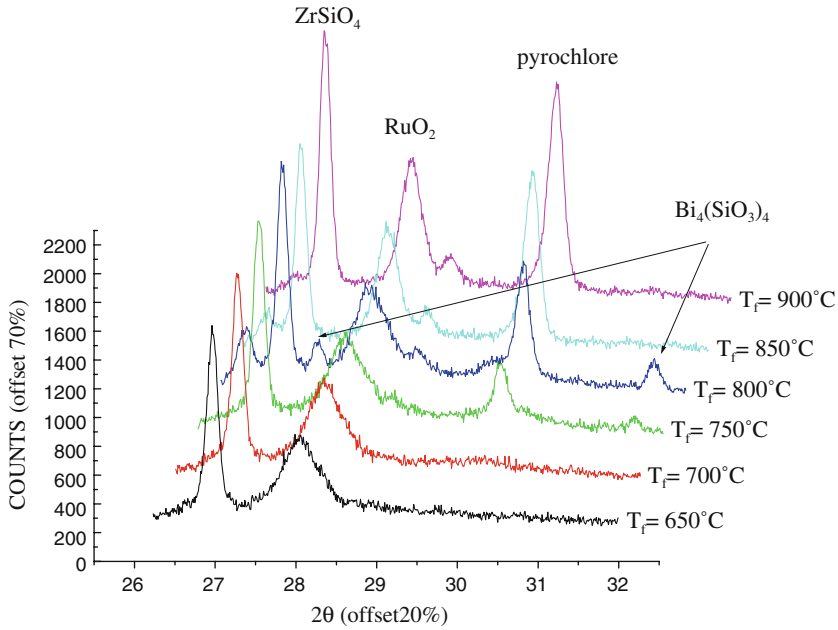

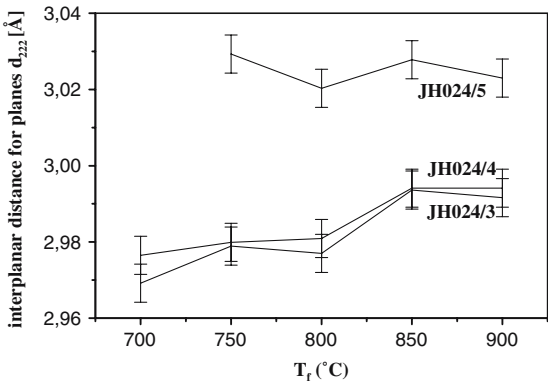


**Fig. 8** Inter-planar distance $d(222)$ as a function of the firing temperature of the pyrochlore phase formed in layers prepared from JH024/3, JH024/4 and JH024/5 inks

Mn, Zn, Zr, Al, Ti, were not completely dissolved in the glassy matrix but remained aggregated in some phases not detected in the XRD analysis. Similar maps have been observed in samples fired from 650 °C up to 900 °C. In particular the elemental maps show the following features:

Bismuth and titanium: The high concentration of Bi in the glass resulted in the detection of Bi over the entire area analysed, but higher amounts of Bi were observed in regions rich in Ti.

Zirconium and silicon: Regions rich in Zr were also rich in Si. Regions poor in Si did not correspond to cavities, but to Zn.

Manganese and zinc: These elements were not homogenously distributed, but no particular correlation with other elements was observed. Nevertheless, regions rich in Zn seem complementary to regions poor in Si. This finding appears to contradict the results of the XRD analysis, which showed the presence of $Zn_2SiO_4$. However we can reconcile the contradiction by assuming that this phase is made up of widely separated grains that were not included in the small area analysed in the experiment.

*JH024/5*

These samples exhibited compositional maps similar to the previous ones, with two exceptions: there were no regions rich in Zr, and in the sample prepared at $T_f = 800°C$ there were crystals of niobium oxide (Fig. 13).

The layers prepared with composition JH024/5 were the most porous ones among the samples investigated, for any firing temperature.

Finally, we observe that no sample displayed a segregated microstructure, i.e., the distribution of conductive grains around grassy regions, which is common in traditional resistors with lead-borosilicate glass.

## 4 Electrical properties

### 4.1 Sheet resistance

Table 3 shows the average values of the sheet resistance $R_\square$ measured with the four-point probe method on layers fired at 850 °C. The table also presents the volume fraction $V_c$ of $RuO_2$ in the three compositions and the relative deviation $\Delta R_\square / R_\square$ from the average values measured on different (at least 10)

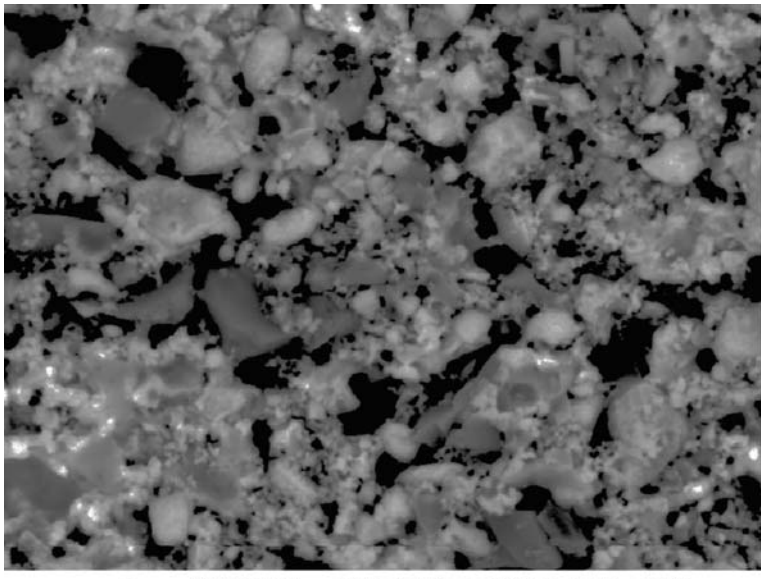


**Fig. 9** BSD-SEM image of the resistive layer prepared with JH024/3 ink

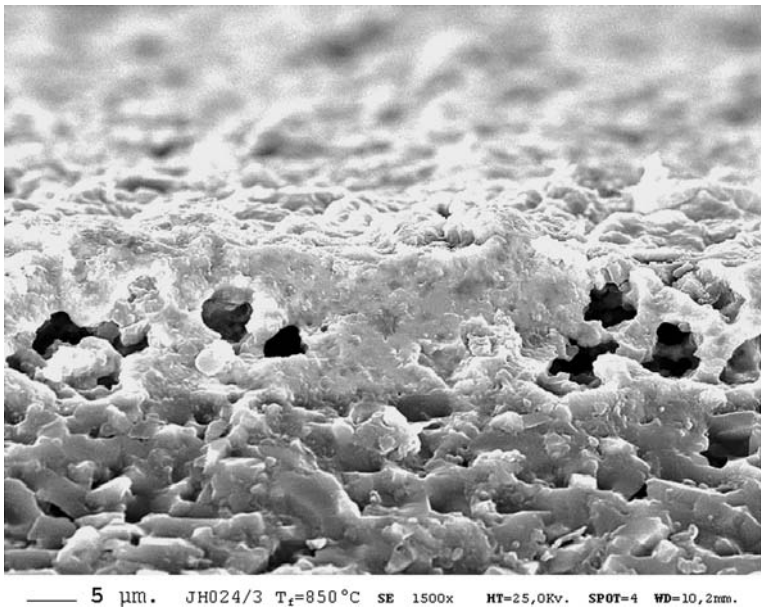


**Fig. 10** SEM-SED image of the cross-section of sample JH024/3 ($T_f$ = 850°C)

points. Data span about two decades of sheet resistance.

Figures 14–16 show the change of the sheet resistance $R_\square$ as a function of the peak firing temperature $T_f$.

Figure 14 shows the temperature dependence of the sheet resistance of sample JH024/3. From 750 to 850°C there is a steep decrease in resistance and from 850 to 900°C the sheet resistance is flat, an indication of very good process sensitivity. In the other two samples (Figs. 15 and 16) the change of sheet resistance $R_\square$ is relatively restricted (less than an order of magnitude), but with a quite irregular behaviour in response to changing the $T_f$ value. The range of values around the average $R_\square$ is wide except at $T_f$ = 850°C. In the temperature range of 825–875°C all samples have very good process sensitivities.

### *4.1.1 TCR*

Plots of $R$ versus $T$ (Fig. 17) for the resistive layers fired at $T_f$ = 850°C (no termination) show the typical

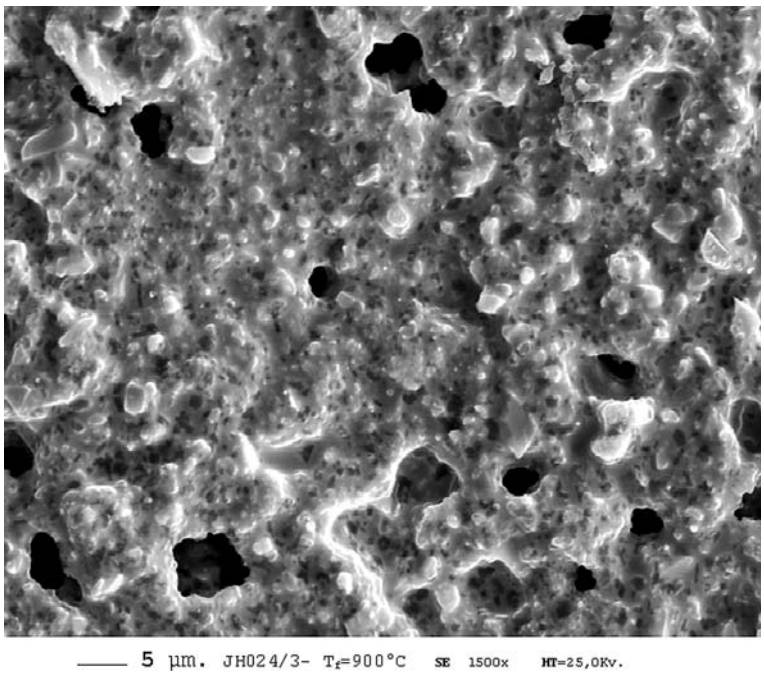


**Fig. 11** SEM-SED image of sample JH024/3 ($T_f$ = 900 °C)

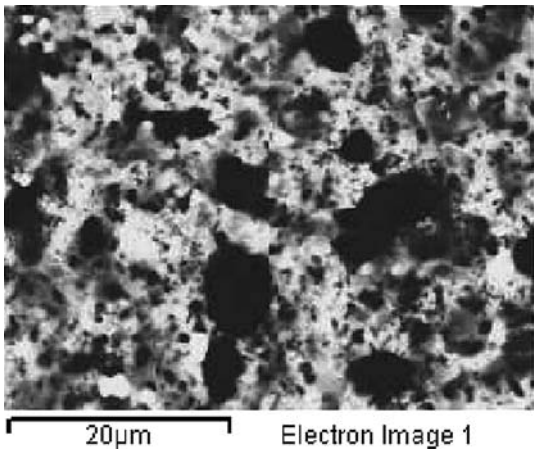


**Fig. 12** SEM-BSD image of the area related to in the following maps

behaviour of TFRs: there is a certain temperature $T_{min}$ at which the resistance displays a minimum value ($R_{min}$). For $T < T_{min}$ the TCR is negative and vice versa for $T > T_{min}$ where the TCR is positive.

Table 4 summarizes the computed values for $T_{min}$, hot TCR (HTCR), cold TCR (CTCR) and the TCR at 20 °C. Table 5 (HTCR) and Table 6 (CTCR) show how the cold and the hot TCR values change with firing temperature.

### 4.2 Size effect (Pt/Au)

The size effect, i.e. the length-dependent effective sheet resistance of TFRs, may result from a change of composition near their terminations. It usually becomes evident in a study of the ''effective $R_{\square}$'' (the

**Fig. 13** JH024/5, $T_f$ = 800°C. SEM-SED image, and elemental map for Nb; $E$ = 15 keV

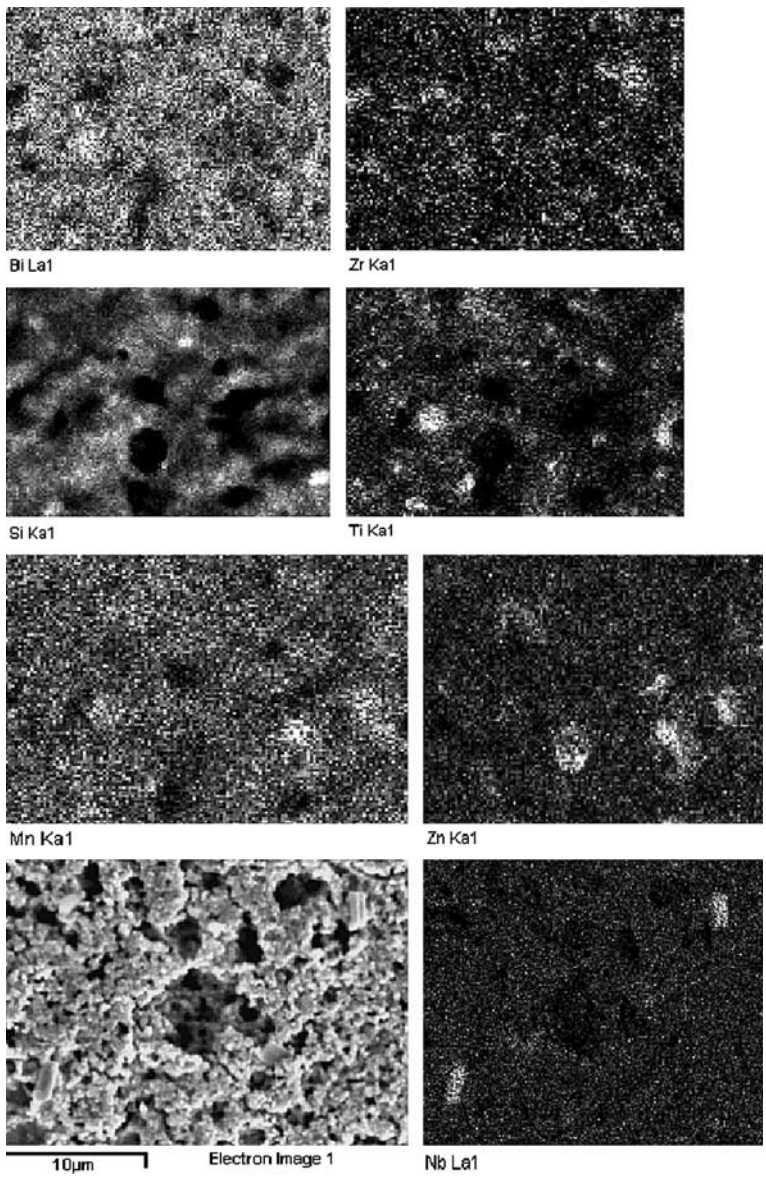

**Table 3** Electrical properties of resistive layers. $T_f$ = 850°C, 10 min

| Resistive layers | $V_C$(%) | $R_\square$ (Ω/□) | $\Delta R_\square/R_\square$ (%) |
|---|---|---|---|
| JH024/3 | 10.1 | 670 | 10 |
| JH024/4 | 17.9 | 68 | 3 |
| JH024/5 | 42.5 | 7.8 | 10 |

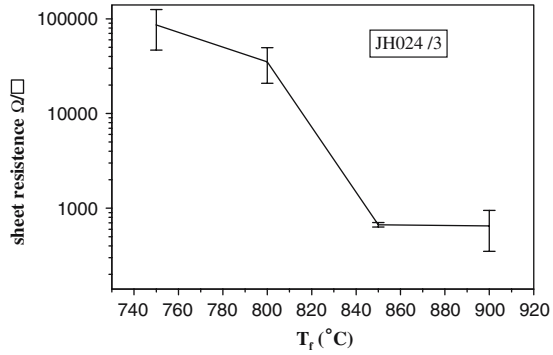


**Fig. 14** $R$ versus $T_f$ for JH024/3

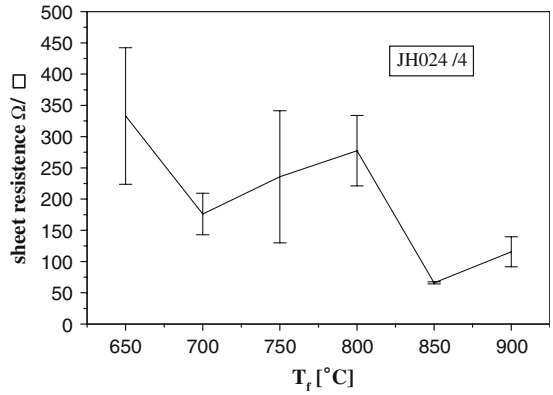


**Fig. 15** Sheet resistance versus $T_f$ for JH024/4

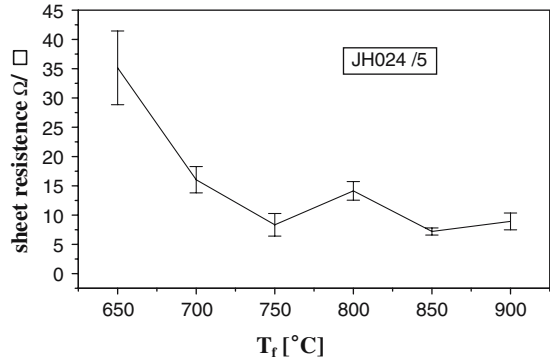


**Fig. 16** Sheet resistance versus $T_f$ for JH024/5

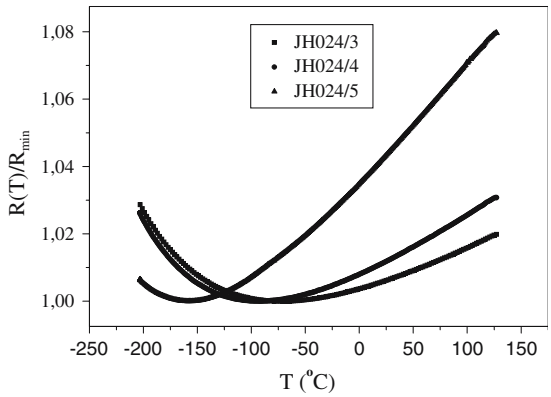


**Fig. 17** $R$ versus T plots for the resistive layers prepared at $T_f$ = 850 °C. The resistance $R$ is normalized to its minimum value $R_{min}$

**Table 4** Values of parameters that describe the temperature dependence of the resistance in the JH024 system, $T_f$ = 850 °C

| Sample | $T_{min}$ [°C] | TCR @ 20 °C [ppm/°C] | HTCR [ppm/°C] | CTCR [ppm/°C] |
|---|---|---|---|---|
| JH024 /3 | – 74 | 110 | 135 | 75 |
| JH024 /4 | – 115 | 160 | 185 | 125 |
| JH024 /5 | – 155 | 340 | 345 | 300 |

**Table 5** HTCR (ppm/°C) for samples fired at various peak temperatures $T_f$

| | $T_f$= 800 °C | $T_f$= 850 °C | $T_f$ = 900 °C |
|---|---|---|---|
| JH024 /3 | – 131 | 135 | 422 |
| JH024 /4 | 111 | 185 | 120 |
| JH024 /5 | 422 | 345 | 292 |

ratio between the actual measured $R$ and the aspect ratio $N_s$ = length divided by width) in a series of resistors prepared in the same way but having various aspect ratios.

Previous studies have shown that a decrease of resistance is often observed (''direct size effect'') [16] near the contacts, but an increase of resistance may also occur (''reverse size effect'') [17]. In our study, resistors were prepared with constant width (2 mm) and different lengths (0.5–10 mm) so that the aspect

**Table 6** CTCR (ppm/°C) for samples fired at various peak temperatures $T_f$

| | $T_f$ = 800 °C | $T_f$ = 850 °C | $T_f$ = 900 °C |
|---|---|---|---|
| JH024 /3 | – 102 | 75 | 70 |
| JH024 /4 | – 52 | 125 | – 56 |
| JH024 /5 | 457 | 300 | 503 |

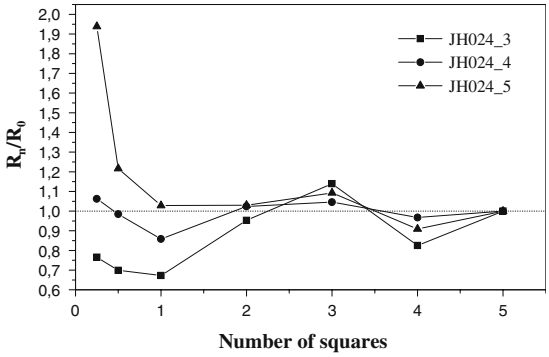


**Fig. 18** Size effects in JH024 resistors with Pt/Au prefired thick film terminations (resistor fired at $T_f$ = 850 °C). $R_o$ represents the sheet resistance of the 10 mm long resistor of the series

ratio changed in the range $N_s$ = 1/4 to $N_s$ = 5. Figure 18 presents the results in terms of the normalized effective sheet resistance, i.e. the effective sheet resistance of each resistor divided by that ($R_o$) of the longest resistor of the series.

The following effects were observed:

(1) A clear inverse size effect in JH024/5 resistors,
(2) a slight direct effect in JH024/3 resistors and
(3) essentially no size effect in resistors JH024/4: (the observed deviations within 10% of short samples may in fact be due to the inevitable difference in their thickness).

The direct size effect observed in the JH024/3 samples suggests that an element diffuses from the termination in the resistor. Further investigations are required to support this hypothesis. The inverse size effect (samples JH024/5), i.e., the increase of resistance near the terminations may be ascribed to the onset of contact resistance [18].

## 5 Summary and conclusions

The study confirms that the chosen bismuthate glass is indeed a suitable matrix for low-resistance $RuO_2$-based lead-free resistors, the only marginal ''defect'' being its poor ability to wet the conductive phase, which results in porous layers. In this respect, the chosen glass composition is inferior to CaBaBAlSi [1] glasses in $RuO_2$-based resistors and in perovskite $CaRuO_3$-based resistors [4]. However, our glass composition gives better performance in terms of reproducibility and TCR values when compared with other model lead-free resistors previously reported [3, 4].

Despite the large fraction of $RuO_2$ in a glassy matrix very rich in Bi, no bismuth ruthenate is formed on firing; on the contrary, a bismuth titanate pyrochlore is the result of interactions between the glass and the additive in the matrix. The smallest deviations of the resistance from the average value are obtained with firing cycles with $T_f$ = 850°C (i.e. with the most common firing conditions used in thick film technology); the same firing conditions give also the most dense films. These performance characteristics, accompanied by the high durability of the glass composition [7] are quite promising, indicating the feasibility of new cadmium free and lead free thick film compositions as substitutes for conventional formulations, to be used in the next generation of hybrid microelectronics.

In conclusion the feasibility of low-sheet resistance $RuO_2$-based lead-free resistors has been demonstrated. Further work is required to better elucidate the ultimate performance characteristics and hopefully the electrical transport mechanisms in this new materials.

## References

1. B. Morten, G. Ruffi, F. Sirotti, A. Tombesi, L. Moro, T. Akomolafe, J. Mat. Sci. Electron. Mater. **2**, 46 (1991)
2. J. Hormadaly, Cadmium-free and lead-free thick-film paste composition, US Patent 5,491,118 (13 Feb 1996)
3. M. Prudenziati, F. Zanardi, B. Morten, A.F. Gualtieri, J. Mater. Sci: Mat. Electron. **13**, 31 (2002)
4. S. Rane, M. Prudenziati, B. Morten, in Proceed. 16th Eur. Microelectronics and Packaging Conf., Prague, (18 June 2004) 277
5. J. Hormadaly, in Proceed. 35th Intl. Symp. on Microelectronics, Colorado (Sept. 4–6, 2002) 543
6. J. Hormadaly, Thick film composition containing pyrochlore-related compounds, US Patent 6,989,111 (24 Jan 2006)
7. J. Hormadaly, Cadmium-free and lead-free glass compositions, thick film formulations containing them and uses thereof , US Patent 6,171,987 B1 (9 Jan 2001)
8. M. Prudenziati, B. Morten, M.L. Brigatti, Active Passive Electron. Comp. **12**, 41 (1985)
9. B. Morten, F. Sirotti, M. Prudenziati, T. Manfredini, J. Phys. D Appl. Phys. **27**, 2227 (1994)
10. A. Taylor, *X-ray metallography* (John Wiley, New York, 1961)
11. S. Piccinini, M. Tamborin, M. Prudenziati, B. Morten, Sens. Actuators **A-58**, 159 (1997)
12. I. Radosavljevic, J.S.O. Evans, A.W. Sleight, J. Solid State Chem. **136**, 63 (1998)
13. X. Wang, H. Wang, X. Yao, J. Am. Ceram. Soc. **80**, 2745 (1997)
14. S.M. Zanetti, S.A. da Silva, G.P. Thim, J. Solid State. Chem. **177**, 4546 (2004)
15. M. Prudenziati, R. Dell'Acqua, in *Thick Film Sensors*, ed. by M. Prudenziati (Elsevier, Amsterdam, 1994), p. 85
16. B. Morten, L. Olumekor, L. Moro, A. Tombesi, J. Phys. D Appl. Phys. **19**, 275 (1986)
17. M. Prudenziati, F. Sirotti, M. Sacchi, B. Morten, A. Tombesi, T. Akomolafe, Active Passive Elec. Comp. **14**, 163 (1991)
18. A. Masoero, B. Morten, M. Prudenziati, A. Stepanescu (1990) Noise in Physical Systems. In: Ambrozy A (ed) Proceed. 10th Intl. Conf., Akademia Kiado Budapest, p 561